ARTICLE

Strong charge polarization effect enabled by surface oxidized titanium nitride for lithium-sulfur batteries

Xiaochun Gao[1], Dong Zhou[1], Yi Chen[1], Wenjian Wu [2], Dawei Su[1], Baohua Li[3,4] & Guoxiu Wang [1]

The commercialization of high-energy-density and low-cost lithium-sulfur batteries has been severely impeded by capacity fading and electrochemical polarization. Here we report a strategy to entrap polysulfides and boost the cathodic redox kinetics by embedding the surface oxidized quantum-dot-size TiN (TiN-O) within the highly ordered mesoporous carbon matrix. While the carbon scaffold offers sufficient electrical contact to the insulate sulfur, benefiting the full usage of sulfur and physical confinement of polysulfides. The surface oxygen renders TiN-O with a strong charge polarization effect for polysulfides via S-O-Ti bond as verified experimentally and theoretically. The suppressed shuttle effect and high lithium ion diffusion coefficient (7.9×10^{-8} cm^2 s^{-1}) lead to a high capacity of 1264 mA h g^{-1} at 0.2 C with a negligible capacity fading rate of 0.06% per cycle. Additionally, TiN-O based prototype soft-package cells also exhibit excellent cycling stability with flexibility, demonstrating their potential for practical applications.

[1] Centre for Clean Energy Technology, Faculty of Science, University of Technology Sydney, Broadway, NSW 2007, Australia. [2] School of Materials Science and Engineering, Dongguan University of Technology, 523106 Guangdong, China. [3] Graduate School at Shenzhen, Tsinghua University, 518055 Shenzhen, China. [4] School of Materials Science and Engineering, Tsinghua University, 100084 Beijing, China. Correspondence and requests for materials should be addressed to D.S. (email: Dawei.Su@uts.edu.au) or to B.L. (email: libh@mail.sz.tsinghua.edu.cn) or to G.W. (email: Guoxiu.Wang@uts.edu.au)

L ithium–sulfur (Li–S) batteries have been considered as one of the most promising next-generation rechargeable battery systems, which can deliver 5 fold higher energy density (theoretical: 2600 Wh kg^{-1}) than the current interaction-based lithium-ion batteries[1,2]. In particular, the natural abundance, environmental friendliness and low cost of sulfur make it more competitive for large-scale energy storage applications[3]. However, Li-S batteries have suffered from the poor capacity retention and sluggish redox kinetics during the solid–liquid–solid lithiation process. The former mainly arises from the "shuttle effect", which is caused by the dissolution and diffusion of lithium polysulfides (Li$_2$S$_n$, $3 \leq n \leq 8$) through the electrolyte, separator and even the anode. The latter is seriously affected by slow mass and electron transfer process due to the low Li$^+$ diffusion rate and poor conductivity of S/Li$_2$S[4–6].

Many efforts have been devoted to addressing these issues, including cathode modification[7,8], electrolyte additives[9,10], interlaid separator[11,12], and anode protection[13]. In the realm of cathodic structure design, carbonaceous hosts with abundant pores and high pore volume showing the capacity of the physical confinement for lithium polysulfides have attracted extensive attentions[14–17]. However, the polysulfides migration driven by concentration diffusion and electrical field cannot be completely prevented, particularly at low rates and over long-term cycling due to the nonpolar feature of the carbon. Therefore, more attentions have been paid on the surface chemistry to strengthen the immobilization and accelerate the redox kinetics of polysulfides. The polar surfaces provided by metal oxides (TiO$_2$, MnO$_2$)[18,19], metal nitrides (VN)[20], metal sulfides (Co$_9$S$_8$)[21], metal phosphides (CoP, FeP)[22,23], and metal carbides (MXene)[24] endow strong polar-polar chemical interactions via dominant chalcogen-lithium binding and minor metal-sulfur binding[25]. Along with strong chemisorption, the unique electrocatalytic effect also triggers multistep redox reactions, leading to higher capacity and Coulombic efficiency[23,26,27]. Cui's group has systematically examined the catalytic effect of metal sulfides (Ni$_3$S, SnS$_2$, FeS, CoS$_2$, VS$_2$, and TiS) in eliminating the overpotential and activation energy barriers between the polysulfides and sulfur[26]. Subsequent research works further explored the catalytically enhanced redox mechanism of metallic Pt particles, W$_2$C[6], Mo$_2$C, TiC[27], VN[20], and CoP[23]. Recently, transition metal nitrides such as TiN, have been intensively investigated, owing to their superior conductivity compared to their oxides and sulfides counterparts, have been largely focused in recent year[28,29]. They even show metallic characteristic, which would be very beneficial to facilitate the redox reaction kinetics and increase the sulfur utilization efficiency for Li–S batteries. Yet the study of polar and conductive TiN as polysulfide mediator for suppressing shuttle effect and boosting redox kinetics needs further investigation as the surface of TiN usually forms a thin oxidization layer in the ambient condition[30], increasing the complexity of understanding the surface chemistry towards the polysulfides redox reaction. Therefore, it is crucial to study polysulfide mediator down to detailed surface interface level.

Herein, we report a rational design on structure and surface chemistry by employing the highly ordered mesoporous carbon (OMC) as matrix and the surface oxidized quantum-dot-size TiN (TiN-O) as polysulfide mediator for suppressing shuttle effect and boosting redox kinetics. The composite with TiN-O embedded in OMC (TiN-O-OMC) not only provides a physical confinement for polysulfides via the narrow-ordered carbon mesoporous channels (with ~3.5 nm pore size distraction), but also chemically immobilizes lithium polysulfides due to the polar surface of the embedded TiN. Our density functional theory (DFT) calculations verify the dramatic charge polarization effect between the polysulfides and surface oxidized TiN-O via the S–O–Ti bond as

verified by the transfer of 1.67e onto TiN-O. Surprisingly, compared to the pure TiN composite, the surface-oxidized TiN-O-OMC shows a stronger affinity for polysulfides with a higher binding energy of -5.51 eV (vs. Li$_2$S$_6$). Moreover, the superior charge polarization effect could impart an additional driving force propelling the electrons gained from anode into the long-chain polysulfides, and attracting lithium ion onto the TiN surface, giving rise to enhanced electron/charge transfer and thus a faster redox kinetics is achieved. The experimental studies show a good consistency that TiN-O-OMC electrode delivers a superior electrochemical catalytic performance with the lowest overpotential of 271 and 465 mV at 0.2 and 5 C and highest lithium ion diffusion coefficient of 3.6×10^{-8} cm^2 s^{-1} (Li$_2$S$_4^{2-} \rightarrow$ Li$_2$S). This rationally designed architecture and surface chemistry of TiN-O leads to a high capacity of 1395 mA h g^{-1} at 0.1 C, a Coulombic efficiency approaching 100% and a high-rate performance of 726 mA h g^{-1} at 5 C. Furthermore, the as-developed sulfur cathode also exhibits great potential for practical applications as demonstrated by the pouch cell with an initial discharge capacity of 845 mA h g^{-1} at 0.2 C and stable cycling performance of 634 mA h g^{-1} after 120 cycles.

Results

Synthesis and material characterization. Metal nitrides are usually synthesized by using the corrosive and hazardous ammonia gas as nitridizing agent. Herein, we demonstrate a green and facile synthetic approach by using g-C$_3$N$_4$ as N source. As illustrated in Fig. 1a, the highly ordered carbon matrix was first synthesized by a nanocasting process, which employs SBA-15 as the hard template and hexamethylenetetramine (HTM) as the precursor. Then TiO$_2$ nanoparticles were generated after the hydrolysis of tetrabutyl titanate (Ti(OC$_4$H$_9$)$_4$) within the OMC. After that, the resultant dark powders were nitridized using g-C$_3$N$_4$ as the upstream N source. Further surface oxidization of TiN was completed by simply exposing the composite in air for 3 days. In addition, control samples carried out without nitriding or natural oxidization process were denoted as TiO$_2$-OMC and TiN-OMC, respectively. The transmission electron microscopy (TEM) observations reveal that the as-prepared OMC successfully replicated highly ordered mesoporous structure of SBA-15 with pores size of approximate 3.5 nm and ~9.9 nm in the wall thickness (Fig. 1b and c). Meanwhile, the ordered mesoporous structure of OMC was well-reserved by TiN-O-OMC after the nanocoating process, which can be seen from the scanning electron microscopy (SEM) images in Fig. 1d, e. The narrow-ordered channels within carbon matrix is speculated to restrain the growth of TiN-O because a homogeneous distribution of quantum-dot-sized TiN-O nanoparticles (3–5 nm) is observed in the high-resolution TEM images (Fig. 1f, g). Similar results are also found in TiO$_2$-OMC and TiN-OMC (Supplementary Fig. 1). Additionally, the non-toxic N-rich g-C$_3$N$_4$ is found to be as effective as NH$_3$ for the nitridization of TiO$_2$. After 3 days air-exposing process, the surface of TiN is easily oxidized as confirmed by the elemental mapping (Fig. 1h and Supplementary Fig. 2).

The sophisticated control of morphology and pore structure was further monitored by small/wide-angle X-ray diffraction (XRD) patterns and N$_2$ adsorption-desorption isotherms (Fig. 2). A distinct diffraction peak indexed to hexagonal (100) reflection is well preserved by TiN-O-OMC after two nanocasting processes (Fig. 2a), revealing its highly ordered structure[31]. Additionally, the slight shifts of the (100) peak towards the higher angle of TiN-O-OMC is ascribed to the structure shrinkage after annealing at elevated temperature and the removal of template[32]. From the wide-angle XRD patterns (Fig. 2b), the typical peaks for both
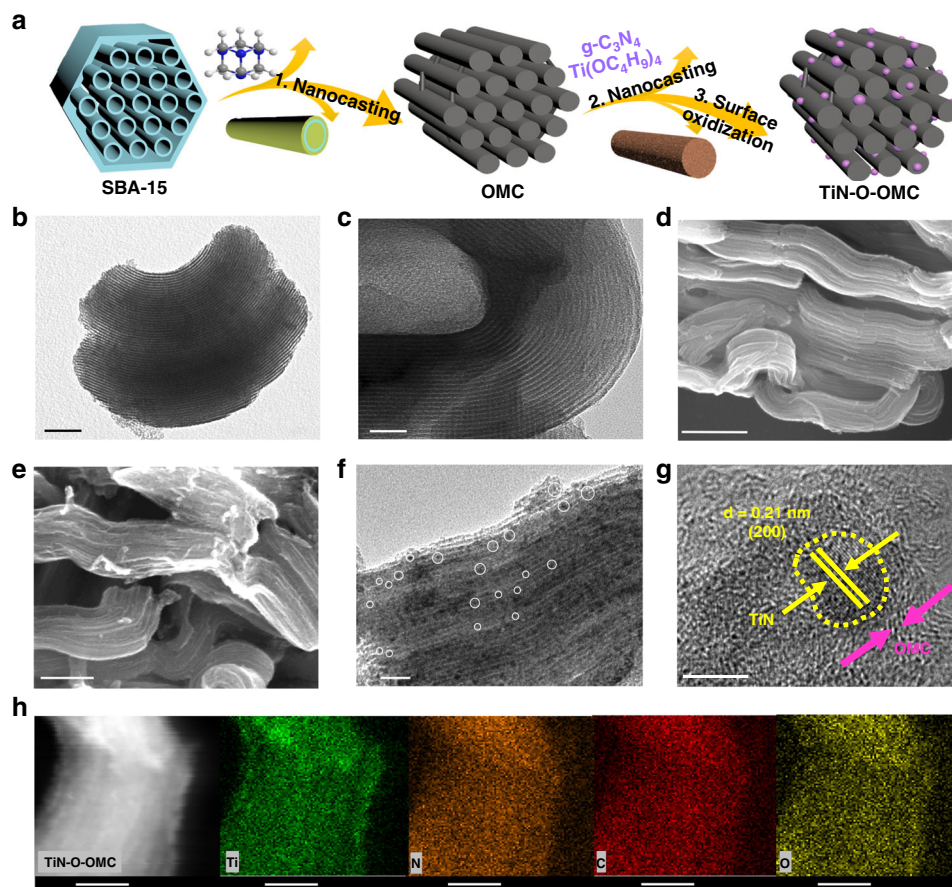
Fig. 1 Synthesis and morphology characterization. **a** Schematic illustration for the fabrication of TiN-O-OMC. TEM images of **b** SBA-15 and **c** OMC. SEM images of **d** OMC and **e** TiN-O-OMC. **f** TEM image and **g** high-resolution TEM image of TiN-O-OMC (lattice fringe of TiN (yellow), OMC (pink)). **h** High-magnification scanning transmission electron microscopy (STEM) image with the corresponding elemental mapping of Ti, N, C, O for TiN-O-OMC. Scale bars: (**b**, **c**) 50 nm, (**d**, **e**) 200 nm, (**f**) 50 nm, (**g**) 5 nm, and (**h**) 100 nm

carbon and TiN can be identified, suggesting the successful nitridization with the assistance of the N-rich g-C$_3$N$_4$[33]. The mesoporous property were further verified by the capillary condensation characterization as shown in Fig. 2c. Similar to SBA-15 and OMC, the N$_2$ adsorption/desorption isotherms of TiN-O-OMC show type IV curve with an H1 hysteresis loop[34]. Additionally, as determined by the Barret-Joyner-Halender (BJH) method, both TiN-O-OMC and OMC demonstrate narrow mesopore size distribution (3.58 and 3.51 nm, respectively), which is consistent with the TEM observation. The control samples, both TiO$_2$-OMC and TiN-OMC also present a consistency of morphology and pore structure (Supplementary Figs. 1, 3–4). Remarkably, the well-designed TiN-O-OMC shows a high Brunauer-Emmett-Teller (BET) surface area of 355.9 m^2 g^{-1} and pore volume of 0.95 cm^3 g^{-1} (Supplementary Table 1), which are critical to providing more active sites and void space to trap and accommodate the sulfur-containing species in Li-S battery. The chemical composition of the TiN-O-OMC surface was identified by X-ray photoelectron spectroscopy (XPS). The molar ratios of 5.8%, 9.6%, 11.8%, and 72.8% were detected for Ti, N, O and C, respectively (Supplementary Table 2). After the natural oxidation process, two new peaks assigned to O-Ti-O and O-Ti-N are deconvolved at 458.5, 464.4 eV and 457.0, 463.1 eV in the Ti 2p spectrum (Fig. 2d). The oxidized species can also be seen from the N 1s and O 1s spectrum (Supplementary Fig. 5). Based on the different fractions of Ti-containing species (Supplementary Table 3) and previous literature[30], the chemical structure of surface oxidized TiN is proposed to contain O-Ti-O top layer,

followed by O-Ti-N intermediate layer and pure TiN in the bulk (Fig. 2e). Additionally, the molar ratio of TiO$_2$/TiN was calculated to be 12:15, indicating that a high portion of surface TiN has converted to TiO$_2$ owing to the natural oxidization.

Electrochemical performance. To examine the effect of surface oxidized TiN on battery performance, systematic electrochemical measurements were conducted using OMC, TiO$_2$-OMC, TiN-OMC and TiN-O-OMC as cathodes with a sulfur content of 75 wt % (Supplementary Fig. 6). After the sulfur infiltration process, no obvious sulfur aggregates are observed (Supplementary Figs. 7–8), indicating sulfur has penetrated into the highly OMC hosts. Fig. 3a and Supplementary Fig. 9 reveal the typical galvanostatic charge/discharge profiles of the sulfur cathodes at different current densities. Two representative discharge plateaus at around 2.38 and 2.10 V are observed (at 0.1 C current rate, 1 C = 1675 mA g^{-1}), corresponding to the reduction of sulfur to long-chain lithium polysulfides (Li$_2$S$_x$, $3 \leq x \leq 8$) and the subsequent formation of short-chain Li$_2$S$_2$/Li$_2$S, respectively[35]. After introducing polar TiO$_2$ and TiN into the OMC matrix, the capacity significantly increases from 710 to 980 and 1264 mA h g^{-1}, respectively (Fig. 3b). Remarkably, TiN-O-OMC electrode delivers the highest specific capacity at different current rates (1395, 1264, 1109, 990, 882, and 727 mA h g^{-1} at 0.1, 0.2, 0.5, 1, 2, and 5 C, respectively, Fig. 3a). Additionally, at a low current rate of 0.2 C, the voltage hysteresis (η) of TiN-OMC is only 1 mV lower than that of TiN-O-OMC, indicating their similar redox kinetics for the solid-liquid-solid lithiation process (Fig. 3c, Supplementary Fig. 9).
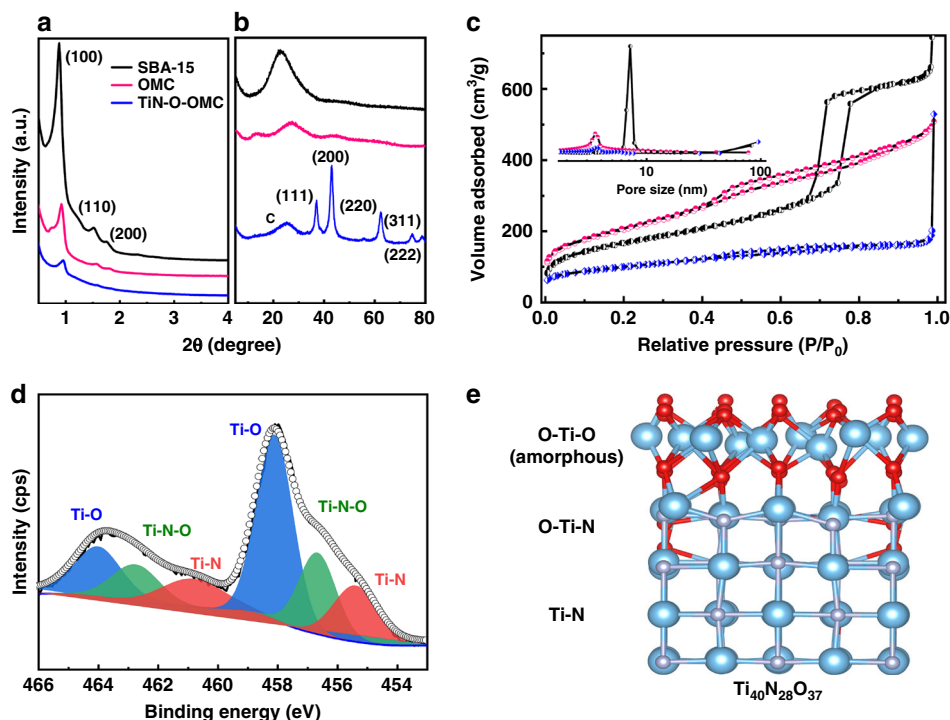
Fig. 2 Structural and surface composition analysis of TiN-O-OMC. **a** Small-angle and **b** wide-angle XRD patterns, **c** N_2 adsorption-desorption isotherms (insert: pore sze distribution plots) of SBA−15 (black), OMC (pink) and TiN-O-OMC (blue). **d** Core-level XPS spectra of Ti 2p of TiN-O-OMC and **e** the proposed chemical structure of surface oxidized TiN

However, at a high current rate of 5 C, η for TiN-OMC, TiO_2-OMC and OMC electrodes are 72, 99, and 215 mV higher than TiN-O-OMC, respectively. Thus, the surface oxidized TiN is particularly effective to alleviate the electrochemical polarization at higher current rate. Benefiting from the mesoporous structure and strong trapping affinity with polysulfides, the TiN-O-OMC electrode demonstrates an excellent high-rate performance. As shown in Fig. 3d, the capacity decreases with the increasing current density and can maintain a high capacity up to $718\,\mathrm{mA\,h\,g^{-1}}$ at 5 C. Furthermore, the capacity can recover to $1284\,\mathrm{mA\,h\,g^{-1}}$ after abruptly switching the current density back to 0.1 C, implying the remarkable robustness and stability of TiN-O-OMC electrode. However, TiN-OMC, TiO_2-OMC, and OMC cathodes deliver much lower capacities after reversing back to low rates, in decreasing order of 992, 553 and $711\,\mathrm{mA\,h\,g^{-1}}$, respectively. For long-term cycling stability at a low current density of 0.2 C (Supplementary Fig. 10), the TiN-O-OMC shows superior cycling stability with a high initial capacity of $1264\,\mathrm{mA\,h\,g^{-1}}$ and a fading rate of 0.06 % from the second cycle. While the capacity fading rates of OMC, TiO_2-OMC and TiN-OMC are 0.14%, 0.17% and 0.13%, respectively. Moreover, at higher current density of 0.5 and 5 C, the capacity of the TiN-O-OMC cathode can maintain at 915 and $612\,\mathrm{mA\,h\,g^{-1}}$ with a negligible fading rate of 0.06 and 0.05% over 200 cycles. The high Columbic efficiency (above 98.2%) indicates the dramatically suppressed shuttle effect of polysulfides. Additionally, we further evaluated the long-term cycling stability of TiN-O-OMC with high sulfur loading ($4.3\,\mathrm{mg\,cm^{-2}}$). It delivers an initial capacity of $645\,\mathrm{mA\,h\,g^{-1}}$ and stable cycling to 600 cycles with a capacity fading rate of 0.2 % at a high current density of 5 C (Supplementary Fig. 11). The high capacity retention of TiN-O-OMC cathodes implies the effective immobilization of lithium polysulfides by the well-designed architecture of surface-oxidized polar TiN embedded in the OMC matrix.

Enhanced redox kinetics. Once the polysulfide is anchored on the polar material, it is essential to trigger the subsequent liquid-to-solid (Li_2S_n to Li_2S) conversion, which is the key to improve the rate performance, maximum the utilization of sulfur species and extending the battery lifespan. To this end, cycling voltammogram (CV) scanning, electrochemical impendence spectroscopy (EIS) and Li_2S nucleation experiments were conducted to study how the surface-oxidized TiN affects the electrochemical process (Fig. 4). As shown in Fig. 4a, TiN-O-OMC electrode shows two cathodic peaks at 2.32 (C1) and 2.04 V (C2) and two anodic peaks at 2.31 (A1) and 2.38 V (A2) at a scan rate of 0.1 $\mathrm{mV\,s^{-1}}$, which is consistent with the Galvanostatic charge/discharge profiles. Additionally, C1, C2 peaks locate at higher potential positions than those of OMC, TiO_2-OMC, and TiN-OMC electrodes, whereas A1and A2 show an opposite tendency (Supplementary Fig. 12), which is in good agreement with the η results (Fig. 3c). The mitigated electrochemical polarization of the TiN-O-OMC electrode is also manifested from the well-separated cathodic/anodic peaks with approximately double the current density than other electrodes. Furthermore, the Li^+ diffusion coefficient (D_{Li^+}, a good descriptor to evaluate the redox kinetics) was measured by CV under different scanning rates from 0.1 to 0.5 $\mathrm{mV\,s^{-1}}$. As seen in Fig. 4b, the cathodic and anodic peaks (I_p) of all the electrodes exhibited a good linear relationship with the square root of scanning rates ($v^{\frac{1}{2}}$), indicating a diffusion-controlled process. Based on the classical Randles-Sevcik Eq. (1):[26]

$$I_p = 268600\ n^{\frac{3}{2}}\ A\ D^{\frac{1}{2}}\ C\ v^{\frac{1}{2}} \tag{1}$$

D_{Li^+} ($\mathrm{cm^2\,s^{-1}}$) can be calculated from the slope of the curve $\left(I_p / v^{\frac{1}{2}}\right)$ as the n (number of electrons transferred in the redox reaction), A (electrode area, $\mathrm{cm^2}$), and C (concentration of Li^+ in the cathode, $\mathrm{mol\,cm^{-3}}$) are unchanged (Fig. 4c). For TiN-O-
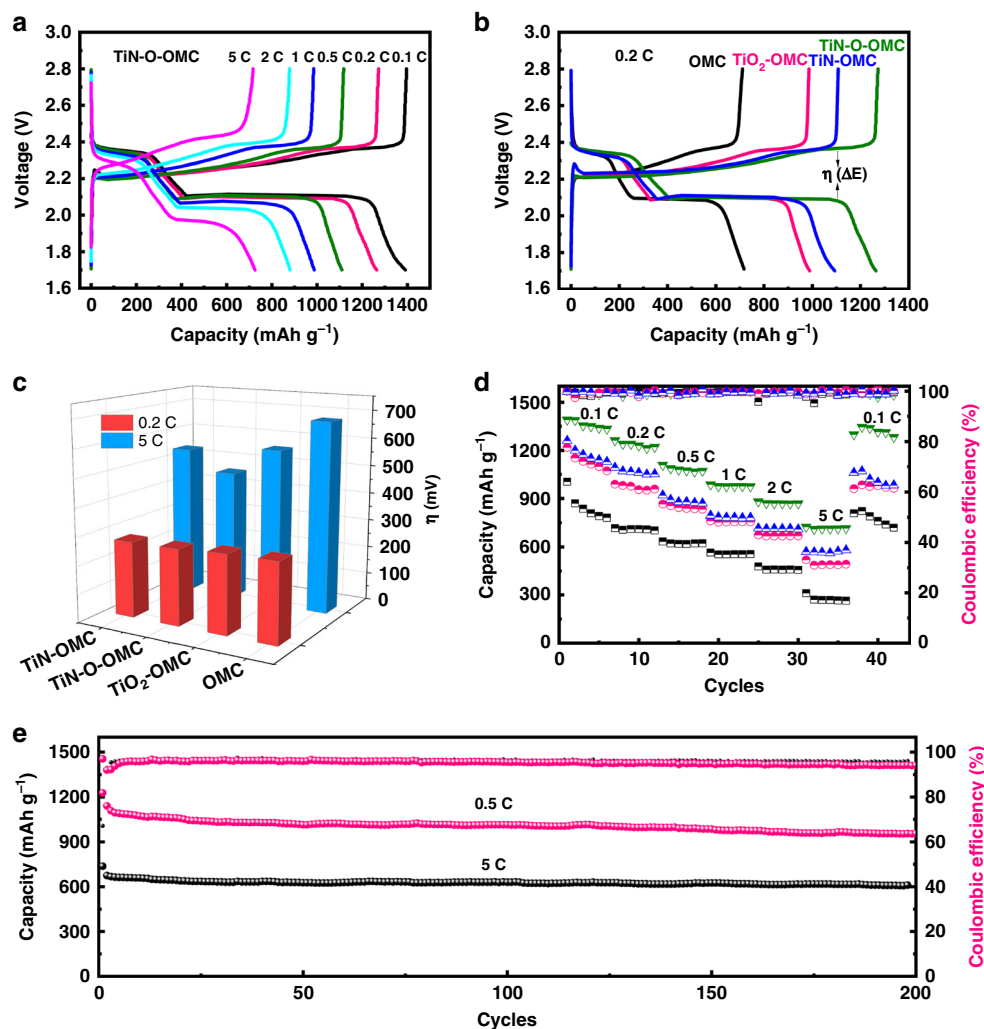
Fig. 3 Electrochemical measurement of Li-S batteries. **a** Galvanostatic charge/discharge profiles of TiN-O-OMC electrode in the range from 0.1 to 5 C. **b** Galvanostatic charge/discharge voltage profiles at 0.2 C for OMC, TiO$_2$-OMC, TiN-OMC and TiN-O-OMC electrodes. **c** The voltage hysteresis (second discharge plateau) of OMC, TiO$_2$-OMC, and TiN-O-OMC, TiN-OMC electrodes at 0.2 and 0.5 C. **d** Comparison of rate performance of OMC (black), TiO$_2$-OMC (pink), and TiN-O-OMC (green), TiN-OMC (blue) electrodes from 0.1–5 C. **e** Cycling stability of TiN-O-OMC at 0.5 C and 5 C

OMC cathode, $D_{Li^+}^{C1} = 1.8 \times 10^{-8}$, $D_{Li^+}^{C2} = 3.6 \times 10^{-8}$, $D_{Li^+}^{A1} = 8.9 \times 10^{-8}$, and $D_{Li^+}^{A2} = 7.9 \times 10^{-8}$ cm^2 s^{-1} are obtained, which are 1–3 times higher than the values for OMC, TiO$_2$-OMC, and TiN-OMC. Without any embedded particles, OMC demonstrated the lowest Li$^+$ diffusivity, indicating its limited surface activity towards the redox reaction. The inferior performance of TiO$_2$-OMC electrode could be ascribed to its large charge transfer resistance confirmed by the EIS result (R$_{ct}$, 90.8 Ω, Fig. 4d and Supplementary Table 4). Surprisingly, although a higher R$_{ct}$ is observed for TiN-O-OMC than TiN-OMC (59.9 Ω vs. 27.3 Ω), the TiN-O-OMC presents higher D$_{Li^+}$ diffusion coefficient than TiN-OMC, which originates from the oxidization layer of TiN. To probe the electrochemical conversion of lithium polysulfides at the electrode/electrolyte interface, symmetric cells employing two identical carbon paper as electrodes (mass loading of 0.4 mg cm^{-2}, without sulfur) and Li$_2$S$_6$ as electrolyte (40 μL of 0.4 M) were assembled[23]. The enhanced current density observed in Fig. 4e proves the fastest lithium polysulfides redox conversion by TiN-O-OMC due to the strong affinity for polysulfides and facilitated ion/electron transport, which has been validated by the adsorption and Li$^+$ diffusion experiments. The EIS spectra further validate the significantly improved conductivity of TiN-containing electrodes (Supplementary Fig. 13).

To further study the favorable effect of the surface oxidized TiN on the polysulfide redox reaction at the liquid-solid boundary, Li$_2$S precipitation experiments on the surface of OMC, TiO$_2$-OMC, TiN-O-OMC, and TiN-OMC were performed[36]. The deposition was studied under galvanostatic discharge to 2.06 V at a constant current of 0.112 mA, which aims to consume most of the long-chain lithium polysulfides[37]. Then, the potentiostatic conditions were applied to maintain an overpotential of 10 mV at 2.05 V till the current fell below 0.01 mA. The 10 mV of overpotential is necessary to provide the driving force for the nucleation of Li$_2$S since a surface energy barrier must be overcome[36]. According to the previous report[36,37], the precipitation of Li$_2$S begins with the nucleation and is then followed by the growth of impingement, as illustrated by the current peak in Fig. 4f and Supplementary Fig. 14. The potentiostatic curves deliver three important data: (i) the current peak increases in the order of OMC < TiO$_2$-OMC < TiN-OMC «-TiN-O-OMC with current densities of 0.12, 0.13, 0.17, and 0.32 mA, (ii) whereas the corresponding disposition time (at current peak) witnesses an opposite tendency of 7489 > 5160 > 5151 > 2709 s, and (iii) the calculated capacities of Li$_2$S precipitation (yellow section) of 45 < 59 < 68 < 95 mA h g$_{sul}^{-1}$ in the same order. The former two values indicate that the fast conversion rate
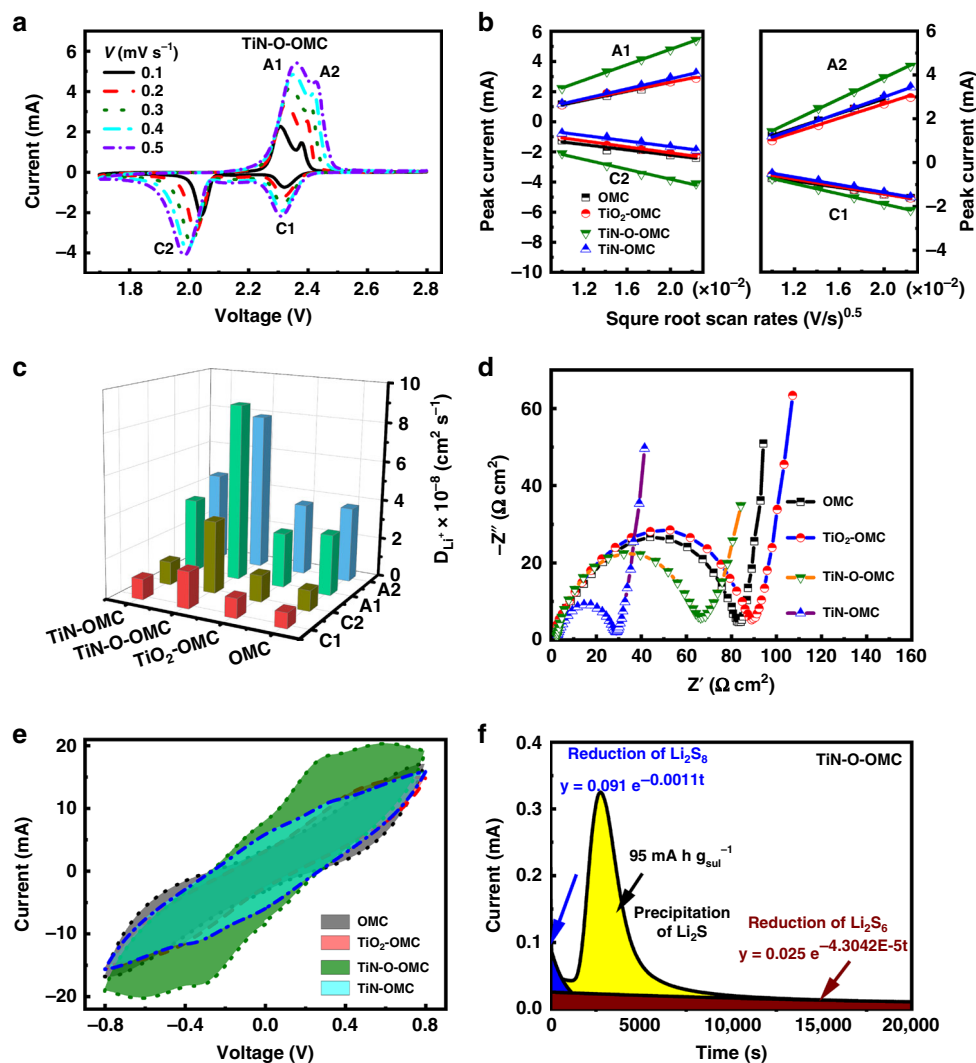
**Fig. 4** Fast redox kinetics and diffusion rate. **a** CV scans of TiN-O-OMC from 0.1–0.5 mV s^{-1} in a typical Li-S coin cell. **b** Peak currents (I_p) versus square root of scan rates ($v^{1/2}$). **c** Calculated Li diffusion coefficient and **d** EIS spectra of OMC, TiO$_2$-OMC, TiN-OMC, and TiN-O-OMC electrodes. **e** CV scans with a 10 mV s^{-1} rate of symmetric cells containing 0.4 M Li$_2$S$_6$ in 1,3-dioxolane (DOL)/1,2-dimethoxyethane (DME, volume ratio 1:1) solution as electrolyte and OMC, TiO$_2$-OMC, TiN-OMC, and TiN-O-OMC as the electrodes. **f** Fitting of current *vs.* time curve for potentiostatic discharge at 2.05 V of TiN-O-OMC based cathode with Li$_2$S$_8$ catholyte

of Li$_2$S nucleation process and the last one reveals the enhanced Li$_2$S deposition process. Therefore, these results clearly elucidate the enhanced electrochemical catalytical property of the naturally oxidized layer of TiN for Li$_2$S conversion than the pure TiN phase.

Enhanced chemical interactions. Ultraviolet–visible (UV–vis) absorption spectroscopy was carried out after immersing the cathode host materials in 5 mM Li$_2$S$_6$ solution to check the trapping effect of lithium polysulfides for surface oxidized TiN. As shown in Fig. 5a, TiN-O-OMC, followed by TiN-OMC, displays the lowest adsorption intensity and completely purify the Li$_2$S$_6$ solution, exhibiting the strongest adsorption affinity for Li$_2$S$_6$. Because of the lower polysulfide binding energy of TiO$_2$ than that of TiN, TiO$_2$-OMC shows lower chemisorption ability with much darker color in Li$_2$S$_6$ solution[38]. In contrast, OMC shows the weakest affinity to Li$_2$S$_6$ owing to the limited binding effect towards Li$_2$S$_6$. Moreover, the strong chemical interaction between the surface oxidized TiN-O-OMC and polysulfide was further confirmed by the XPS spectra after vacuuming the solvent used in adsorption experiment. As verified in Fig. 5b, c, the Ti 2p

and O 1s spectra show a significant 0.2 ~ 1.0 eV shift to the lower binding energy. The enhanced XPS intensity around 456.5 eV might indicate the formation of S-O-Ti binding. To gain more insights into the oxidization effect of TiN, DFT calculations were performed to study the absorption of typical lithium polysulfide, Li$_2$S$_6$, on the TiN (200) crystal facet as reported previously[29]. For a comparison, the binding behavior and chemical interaction of Li$_2$S$_6$ with the pristine TiN was also studied. As shown in Fig. 5d, the terminal S site of Li$_2$S$_6$ tends to locate above the Ti atom while Li atom tends to interact with N atom with the binding lengths of 2.43 and 1.98 Å, respectively. Whereas, for the oxidized TiN, S sites preferentially stand away from the surface while Li atom shows a shorter binding length of 1.89 Å to O atom, predicting a stronger binding affinity. This is further confirmed by the higher binding energy (E_b) of surface oxidized TiN (-5.51 eV) than that of pure TiN (-5.39 eV), which is consistent with the existing experimental observations. Moreover, the O atoms are favorable in the charge polarization effect due to the larger electronegativity of oxygen, which is widely studied in the field of hetero-atom doping[39,40]. As depicted from the charge density difference diagrams (Fig. 5f, g), the olive and cyan iso-surfaces represent the
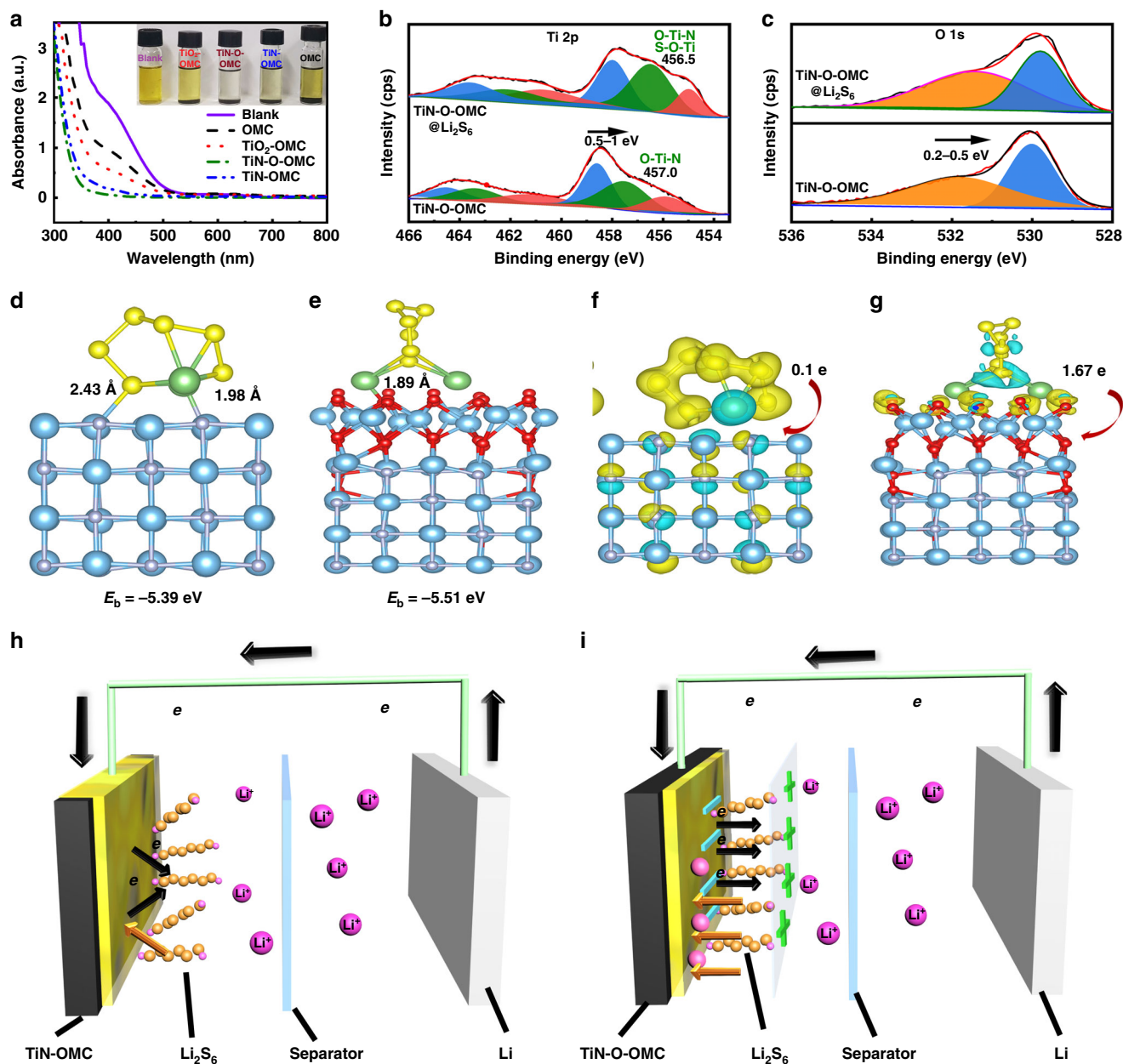
Fig. 5 Demonstration of the strong chemical interactions. **a** Ultraviolet/visible adsorption spectra of 5 mM Li_2S_6 in DOL/OME (volume 1:1) after the addition of 5 mg OMC, TiO_2-OMC, TiN-O-OMC and TiN-OMC (insert: digital photo of Li_2S_6 solutions after the addition of host materials). **b** High-resolution XPS spectrum of Ti 2p and **c** O 1s before and after immersing in 5 mM Li_2S_6 solution acquired from TiN-O-OMC. Optimized configurations for the binding of Li_2S_6 to **d** TiN **e** TiN-O. Charge density difference diagrams of **f** TiN and **g** TiN-O. Blue, gray, red, green, and yellow balls represent Ti, N, O, Li and S atoms, respectively. The cyan and yellow colors indicate the regions of charge loss and gain. **h**, **i** Schematic illustration of the enhanced charge/electron transport of TiN-O-OMC over TiN-OMC

region of net electron accumulation and deficit, respectively. In details, a limited 0.1*e* is transferred from the long-chain Li_2S_6 to pure TiN, whereas 1.67*e* is transferred to the surface oxidized TiN. The significant polarization of electronic density is also in good accordance with the negative shifting (0.2~1 eV) of Ti 2p and O 1s XPS spectra (Fig. 5b–c). It can be inferred that in the discharge process, the enhanced electronic polarization effect could provide an additional driving facilitate to profit the electrons transfer from anode to polysulfides, attract Li^+ onto the surface of TiN-O-OMC and accelerate charge/electron transport (as illustrated in Fig. 5h, i).

Motivated by the urgent demand for developing flexible future energy storage devices, herein we manufactured prototype pouch

cells, employing the as-prepared TiN-O-OMC as the cathode material with a sulfur loading of ~1.4 mg cm^{-2} and a size of 60 mm × 80 mm (Fig. 6a and Supplementary Fig. 15). This unique pouch cell demonstrates superior flexibility by adapting to different folding movements from 0 to 180° (Fig. 6b, Supplementary Movie 1). Benefiting from the enhanced physiochemical adsorption ability for lithium polysulfides and fast redox kinetics, the TiN-O-OMC in pouch cells also shows a high specific capacity of 884, 788, 727, 650, and 550 mA h g^{-1} at 0.1, 0.2, 0.5, 1, and 2 C, respectively, and a low η of 239 mV at 0.2 C (Fig. 6c and Supplementary Fig. 16). In addition, the TiN-O-OMC pouch cell exhibits an excellent rate performance that the capacity can recover to 790 mA h g^{-1} after decreasing the current density from
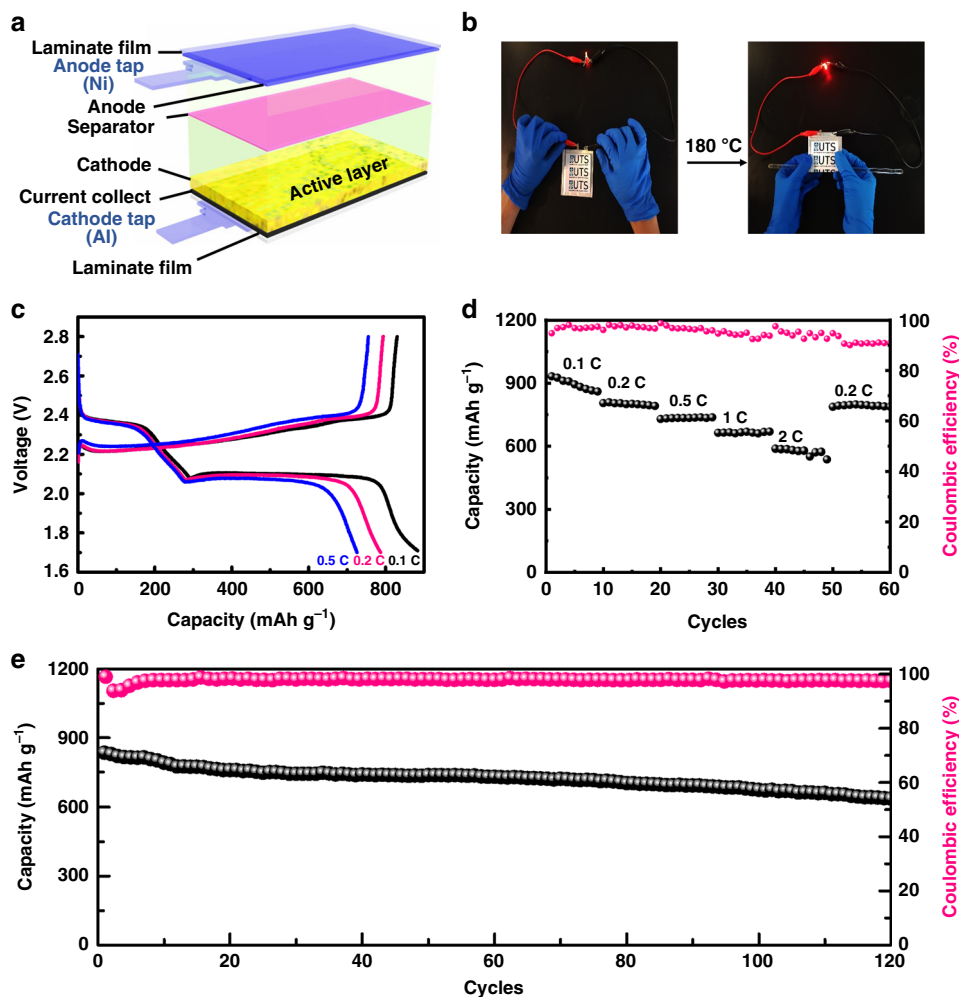
Fig. 6 Pouch cell performance of TiN-O-OMC@S cathode. **a** Schematic of the basic configuration of a proof-of-concept Li-S pouch cell. **b** Flexibility test with folding angles from 0 to 180° of the as-prepared TiN-O-OMC pouch cell. **c** Galvanostatic charge/discharge profiles at low rates of 0.1, 0.2, and 0.5 C. **d** Rate performance and Coulombic efficiency at different current densities. **e** Cycling stability and Coulombic efficiency at 0.2 C with a sulfur loading of 1.4 mg cm^{-2}

2 to 0.2 C (Fig. 6d). Notably, the cathode displays a stable cycling performance with a high capacity retention of 634 mA h g^{-1} (at a low fading rate of 0.16% per cycle) and high Columbic efficiency of 98.5% at 0.2 C (Fig. 6e). When tested at a high sulfur loading of ~4.3 mg cm^{-2}, the pouch cell shows a capacity of 552 mA h g^{-1} and a good cycling stability with a fading rate of 0.06% after the third cycle (Supplementary Fig. 17). The state-of-art pouch cells with TiN-O-OMC as cathode material can drive a mini electric car as demonstrated in Supplementary Movie 2, further indicating the potential for practical application.

Discussion
In summary, we successfully developed a technique by employing the highly OMC as matrix and the surface oxidized quantum-dot-size TiN-O as polysulfide mediator to suppress shuttle effect and boost redox kinetics of Li–S batteries. Both the physical confinement and chemical adsorption for the polysulfides of the as-prepared materials facilitate the redox reaction between sulfur and polysulfides. Especially, the surface oxidized TiN-O is more effective in alleviating the polysulfides shuttle effect and boosting the overall redox kinetics, which has been confirmed by both experimental and theoretical studies. The DFT calculations further verified that the surface oxygen renders a charge polarization effect for imparting additional "driving force" to propel

both the electrons and Li$^+$ transportation. Benefiting from the synergetic effects of mesoporous architecture and oxidized surface chemistry, the TiN-O-OMC cathode exhibits significant enhancement on the charge transfer process, lower polarization (271 mV), high lithium ion diffusion coefficient (7.9 × 10^{-8} cm^2 s^{-1}) and Li$_2$S nucleation/deposition conversion. Thus, the TiN-O-OMC electrode achieves high specific capacities of 1395 and 726 mA h g^{-1} at 0.1 and 5 C and high Coulombic efficiencies (~100%). The cathode material also delivers excellent rate performance and cycling stability. When assembling to the prototype pouch cells, the as-prepared materials show a superior flexibility with high capacity of 890 mA h g^{-1} at 0.2 C and stable cycling performance of 634 mA h g^{-1} after 120 cycles, indicating great potential for practical applications.

Methods
Synthesis of OMC. In a typical synthesis, 1 g SBA-15[32] and 10 g of HTM (Sigma-Aldrich, 99.0%) were well-dispersed in 20 mL of deionized water. The solution was then vacuumed at room temperature for 2 h and stirred for another 3 h. After centrifugation (9000 rpm, 3 min), the collected paste was further heated at 60 °C for 12 h and annealed at 750 °C for 6 h under Ar stream with a heating rate of 3 °C min^{-1}. Finally, the black carbonaceous product was obtained after a 5% HF (Sigma-Aldrich, 40–45%) solution etching process.

Synthesis of titanium nitride/oxide-carbon composites. Specifically, 100 mg of OMC was added to 4 mL of ethanol (Sigma-Aldrich, 99.8%)/tetrabutyl titanate

(Aldrich, 97%) (1:1, volume ratio) solution, followed by a sonication for 30 min. The suspension was then vacuumed for 20 min to allow a complete infiltration of tetrabutyl titanate. After centrifugation (9000 rpm, 3 min), the black paste was spread on a petri dish and exposed to air for 1 day to allow a completed hydrolysis of tetrabutyl titanate within OMC matrix. Then, the solid was ground and transferred to a boat which 80 mg of g-C_3N_4[41] was in the upstream. The mixture was further heated at 800 ºC for 3 h with a heating rate of 3 ºC min^{-1}. The black TiN-O-OMC powder was finally obtained after a cooling process and a subsequent air exposure for 3 days. A control sample of TiN-OMC was immediately collected from the tube furnace and preserved in an air-free glovebox. While TiO_2-OMC was prepared via the similar procedure as that of TiN-O-OMC except for the absence of g-C_3N_4 as N source in the annealing process.

Synthesis of TiN-O-OMC cathodes. In this work, sulfur was loaded by a melt-diffusion strategy. Typically, 25 wt% of TiN-O-OMC and 75 wt% of sulfur (Sigma-Aldrich, 99.5%) was ground together till the mixture show a good color uniformity. The solid was transferred to a small glass tube sealed with polyethylene wrap and heated at 155 ºC for 12 h. Then, 80 mg of the TiN-O-OMC/S composite, 10 mg of acetylene carbon black and 10 mg of poly(vinylidene fluoride) (PVDF, $(CH_2CF_2)_n$) were mixed with 500 μL of N-methyl-2-pyrrolidone (NMP) to form a uniform slurry. The slurry was coated on an Al foil and then dried in a vacuum oven at 60 ºC overnight. The Al foil was then punched into 12 mm diameter disks and the sulfur loading was controlled in the range of 1.2–1.6 mg cm^{-2}. For comparison experiments, OMC, TiO_2-OMC, and TiN-OMC electrodes were also prepared under the same condition.

Material characterization. Field-emission SEM (Zeiss Supra 55VP) and TEM (JEM-2011) were applied to record the morphologies of the samples. XRD patterns (Bruker D8 Discovery) and N_2 adsorption and desorption isotherms (Micromeritics 3 Flex) were obtained to analyse the ordered structure. XPS (ESCA-LAB250Xi) with a monochromatic Al Kα source and elements mapping were used to probe the chemical compositions of the samples. The thermogravimetric analysis (TGA, SDT2960) was carried out on simultaneous thermal-gravimetry and differential thermal analysis with a heating rate of 5 ºC min^{-1} under N_2 atmosphere. UV–vis adsorption spectral analysis (Cary 60) was performed to study the adsorption of Li_2S_6.

Electrochemical measurements. To evaluate the electrochemical performance of TiN-OMC, 2030-type coin cells were assembled using lithium metal as anode and reference electrode, and Celgard 2300 as the separator. The cells were assembled in an Ar-filled glove box (UniLab, Mbraun, Germany) with low levels of both H_2O and O_2 (0.1 ppm). A freshly prepared solution containing 1 M lithium bis-(trifluoromethanesulfonyl) imide (LiTFSI, 99.95%) and 1 wt% $LiNO_3$ in DOL/DME (volume ratio 1:1) was used as electrolyte. The cells were operated in a voltage range of 1.7–2.8 V with Neware battery tester. Cyclic voltammetry was recorded on a Bio-Logic VMP3 electrochemical workstation in the voltage range of 1.7–2.8 V. EIS was tested in the frequency range between 0.01 Hz and 100 kHz.

Li_2S_6 adsorption test. The Li_2S_6 solution (5 mM) was prepared by dissolving Li_2S and sulfur in a DOL/DME mixed solution (1:1, volume ratio) with a molar ratio of 1:5 at 80 ºC for 24 h. Afterward, 5 mg of the as-prepared samples was added into the Li_2S_6 solution, followed by a soaking, standing process. Finally, 3 mL of the clear upper solution was taken out for the UV-visible adsorption test.

Assembly of Li_2S_6 symmetric cells and measurement. Two identical carbon paper disks (1.2 cm in diameter) were used as current collectors to load the as-prepared host materials. The well-sonicated suspension of materials and ethanol was drop-cast on carbon paper with a mass loading of 0.35 mg cm^{-2}. Celgard 2300 was used as a separator and 0.5 M Li_2S_6 was used as the electrolyte. Particularly, the TiN-OMC electrodes were prepared in the Ar-filled glove box to prevent the surface oxidation of TiN. Both CV and EIS experiments were performed with a Bio-Logic VMP3 Multi Potentiostat.

Li_2S nucleation measurements. The 0.4 M Li_2S_8 catholyte was firstly synthesized by stirring the Li_2S with sulfur at a molar ratio of 1:7 in tetraglyme in the glovebox for 8 h at room temperature[29]. Accordingly, the cathodes were the same with those as mentioned in the symmetric cells experiment while lithium foils were used as anodes. For the 2030-type coin cells assembly, 20 μL Li_2S_8 catholyte was firstly added to the cathode, followed by a Celgard 2300 separator and another 20 μL Li-S electrolyte on the top. The batteries were galvanostatically discharged to 2.06 V under 0.112 mA and then held at voltage 2.05 V until the current was below 0.01 mA. Based on Faraday's law, the nucleation/growth of Li_2S can be evaluated via the fitting of current-time curves after the second potentiostatically discharge stage.

Assembly of pouch cells. The laminate film with 16 × 20 cm size was first half-folded and sealed by the hot-sealing machine as the shell of pouch cell. The pouch cell cathode electrodes were prepared with the same procedures as those electrodes prepared for coin cells but with a larger size of 6 × 8 cm. The Al tab was welded

onto the cathode electrode. Then, the cathode was sticked the Celgard 2300 separator by the anti-electrolyte-tape. Afterwards, the Li foil anode was pasted on the separator with anti-electrolyte-tape in glovebox with welded Ni tap. Then both the cathode and Li foil anode were put in the laminate film package and side sealed by the hot-sealing machine. Then 1.2 g of Li–S electrolyte was injected into the package through the unsealed side. After that, the package was vacuumed and sealed via the vacuum sealing machine. After standby for 1 day, the pouch cell was pressed by formation machine and activated by discharging and charging to 1.7 and 2.8 V at a low current density of 0.2 C. After for another 12 h, the pouch cell was electrochemically tested using the Land Workstation (see Supplementary Fig. 15a–g).

DFT calculations. The first principle calculations were conducted using spin-polarized Perdew-Burke-Ernzerhof (PBE) exchange-correlation functional by Vienna Ab initio Simulation Package (VASP)[42,43]. The Grimme DFT-D2 method was applied to treat the van der Waals force between Li_2S_6 and TiN /TiN-O. There are more than 100 atoms in TiN-O structure with relaxed lattice constants 8.488 Å, and the vacuum gap is more than 20 Å. For the initial structure, many possible stacking patterns and distances between Li_2S_6 and TiN were tested to obtain the stable configuration. The kinetic cutoff energy is set 400 eV, while the Γ-centered Monkhorst–Pack grid is 2 × 2 × 1. The convergence of force of each atom was 0.05 eV Å^{-1}. The binding energy (E_b) is calculated using Eq. (2):

$$E_b = E(Li_2S_6 + TiN - O) - E(Li_2S_6) - E(TiN - O) \qquad (2)$$

where the E (Li_2S_6 + TiN-O) presents the total energy for optimized configuration of Li_2S_6 and TiN-O complex, and the E (Li_2S_6) and E (TiN-O) present the energies for optimized isolated Li_2S_6 and TiN-O structures, respectively. All the crystal structures and charge density plots were drawn using ESTA.

Data availability

The data that support the findings of this study are available from the corresponding author upon reasonable request.

References

1. Seh, Z. W., Sun, Y., Zhang, Q. & Cui, Y. Designing high-energy lithium-sulfur batteries. *Chem. Soc. Rev.* **45**, 5605–5634 (2016).
2. Li, G. et al. Chemisorption of polysulfides through redox reactions with organic molecules for lithium-sulfur batteries. *Nat. Commun.* **9**, 705 (2018).
3. Saha, N. C. & Tompkins, H. G. Titanium nitride oxidation chemistry: an x-ray photoelectron spectroscopy study. *J. Appl. Phys.* **72**, 3072–3079 (1992).
4. Hu, C. et al. In situ wrapping of the cathode material in lithium-sulfur batteries. *Nat. Commun.* **8**, 479 (2017).
5. Li, Z. et al. A highly ordered meso@ microporous carbon-supported sulfur@ smaller sulfur core-shell structured cathode for Li-S batteries. *ACS Nano* **8**, 9295–9303 (2014).
6. Thangavel, N. K., Gopalakrishnan, D. & Arava, L. M. R. Understanding heterogeneous electrocatalysis of lithium polysulfide redox on Pt and WS_2 surfaces. *J. Phys. Chem. C* **121**, 12718–12725 (2017).
7. Yang, Y. et al. Rational design of hierarchical TiO_2/epitaxially aligned MoS_2-carbon coupled interface nanosheets core/shell architecture for ultrastable sodium-ion and lithium-sulfur batteries. *Small Methods* **2**, 1800119 (2018).
8. Wang, H. et al. Tailored reaction route by micropore confinement for Li–S batteries operating under lean electrolyte conditions. *Adv. Energy Mater.* **8**, 1800590 (2018).
9. Huang, J.-K. et al. Functional two-dimensional coordination polymeric layer as a charge barrier in Li-S batteries. *ACS Nano* **12**, 836–843 (2018).
10. Fan, L., Wei, S., Li, S., Li, Q. & Lu, Y. Recent progress of the solid-state electrolytes for high-energy metal-based batteries. *Adv. Energy Mater.* **8**, 1702657 (2018).
11. Jeong, Y. C., Kim, J. H., Nam, S., Park, C. R. & Yang, S. J. Rational design of nanostructured functional interlayer/separator for advanced Li-S batteries. *Adv. Funct. Mater.* **28**, 1707411 (2018).
12. He, J., Chen, Y. & Manthiram, A. Vertical Co_9S_8 hollow nanowall arrays grown on Celgard separator as a multifunctional polysulfide barrier for high-performance Li-S batteries. *Energy Environ. Sci.* **11**, 2560–2568 (2018).
13. Pang, Q. et al. Tuning the electrolyte network structure to invoke quasi-solid-state sulfur conversion and suppress lithium dendrite formation in Li-S batteries. *Nat. Energy* **3**, 783 (2018).
14. Xin, S. et al. Smaller sulfur molecules promise better lithium-sulfur batteries. *J. Am. Chem. Soc.* **134**, 18510–18513 (2012).

15. Li, D. et al. High sulfur loading cathodes fabricated using peapodlike, large pore volume mesoporous carbon for lithium-sulfur battery. *ACS Appl. Mater. Interface* **5**, 2208–2213 (2013).

16. Liang, X. & Nazar, L. F. In situ reactive assembly of scalable core-shell sulfur-MnO$_2$ composite cathodes. *ACS Nano* **10**, 4192–4198 (2016).

17. Ji, X., Lee, K. T. & Nazar, L. F. A highly ordered nanostructured carbon–sulphur cathode for lithium-sulphur batteries. *Nat. Mater.* **8**, 500–506 (2009).

18. Qiu, J. et al. Photocatalytic synthesis of TiO$_2$ and reduced graphene oxide nanocomposite for lithium ion battery. *ACS Appl. Mater. Interface* **4**, 3636–3642 (2012).

19. Kong, W. et al. Ultrathin MnO$_2$/graphene oxide/carbon nanotube interlayer as efficient polysulfide-trapping shield for high-performance Li-S batteries. *Adv. Funct. Mater.* **27**, 1606663 (2017).

20. Song, Y. et al. Synchronous immobilization and conversion of polysulfides on a VO$_2$-VN binary host targeting high sulfur load Li-S batteries. *Energy Environ. Sci.* **11**, 2620–2630 (2018).

21. Chen, T. et al. Metallic and polar Co$_9$S$_8$ inlaid carbon hollow nanopolyhedra as efficient polysulfide mediator for lithium-sulfur batteries. *Nano Energy* **38**, 239–248 (2017).

22. Huang, S. et al. Regulating the polysulfide redox conversion by iron phosphide nanocrystals for high-rate and ultrastable lithium-sulfur battery. *Nano Energy* **51**, 340–348 (2018).

23. Zhong, Y. et al. Surface chemistry in cobalt phosphide-stabilized lithium-sulfur batteries. *J. Am. Chem. Soc.* **140**, 1455–1459 (2018).

24. Bao, W., Su, D., Zhang, W., Guo, X. & Wang, G. 3D metal carbide@mesoporous carbon hybrid architecture as a new polysulfide reservoir for lithium-sulfur batteries. *Adv. Funct. Mater.* **26**, 8746–8756 (2016).

25. Pang, Q., Liang, X., Kwok, C. Y. & Nazar, L. F. Advances in lithium-sulfur batteries based on multifunctional cathodes and electrolytes. *Nat. Energy* **1**, 16132 (2016).

26. Zhou, G. et al. Catalytic oxidation of Li$_2$S on the surface of metal sulfides for Li-S batteries. *Proc. Natl Acad. Sci. USA* **114**, 840–845 (2017).

27. Zhou, F. et al. Low-cost metal carbide nanocrystals as binding and electrocatalytic sites for high performance Li-S batteries. *Nano Lett.* **18**, 1035–1043 (2018).

28. Cui, Z., Zu, C., Zhou, W., Manthiram, A. & Goodenough, J. B. Mesoporous titanium nitride-enabled highly stable lithium-sulfur batteries. *Adv. Mater.* **28**, 6926–6931 (2016).

29. Zhou, T. et al. Twinborn TiO$_2$-TiN heterostructures enabling smooth trapping-diffusion-conversion of polysulfides towards ultralong life lithium-sulfur batteries. *Energy Environ. Sci.* **10**, 1694–1703 (2017).

30. Esaka, F. et al. Comparison of surface oxidation of titanium nitride and chromium nitride films studied by X-ray absorption and photoelectron spectroscopy. *J. Vac. Sci. Technol. A* **15**, 2521–2528 (1997).

31. Park, S. S., Chu, S.-W., Xue, C., Zhao, D. & Ha, C.-S. Facile synthesis of mesoporous carbon nitrides using the incipient wetness method and the application as hydrogen adsorbent. *J. Mater. Chem.* **21**, 10801 (2011).

32. Gao, X. et al. Cosolvent-free nanocasting synthesis of ordered mesoporous g-C$_3$N$_4$ and its remarkable photocatalytic activity for methyl orange degradation. *RSC Adv.* **5**, 76963–76972 (2015).

33. Sun, P. et al. Rational design of carbon shell endows TiN@C nanotube-based fiber supercapacitors with significantly enhanced mechanical stability and electrochemical performance. *Nano Energy* **31**, 432–440 (2017).

34. Chen, J. et al. Nano-sized TiN on carbon black as an efficient electrocatalyst for the oxygen reduction reaction prepared using a mpg-C$_3$N$_4$ template. *Chem. Commun.* **46**, 7492–7494 (2010).

35. Ji, X., Lee, K. T. & Nazar, L. F. A highly ordered nanostructured carbon–sulphur cathode for lithium-sulphur batteries. *Nat. Mater.* **8**, 500–506 (2009).

36. Fan, F. Y., Carter, W. C. & Chiang, Y. M. Mechanism and kinetics of Li$_2$S precipitation in lithium-sulfur batteries. *Adv. Mater.* **27**, 5203–5209 (2015).

37. Xu, J. et al. Promoting lithium polysulfide/sulfide redox kinetics by the catalyzing of zinc sulfide for high performance lithium-sulfur battery. *Nano Energy* **51**, 73–82 (2018).

38. Wang, Y. et al. Carbon@titanium nitride dual shell nanospheres as multi-functional hosts for lithium sulfur batteries. *Energy Storage Mater.* **16**, 228–235 (2019).

39. Gao, X., Wang, L., Ma, J., Wang, Y. & Zhang, J. Facile preparation of nitrogen-doped graphene as an efficient oxygen reduction electrocatalyst. *Inorg. Chem. Front.* **4**, 1582–1590 (2017).

40. Jiang, L. et al. Doping of graphitic carbon nitride for photocatalysis: a review. *Appl. Catal. B Environ.* **217**, 388–406 (2017).

41. Wang, X. et al. A metal-free polymeric photocatalyst for hydrogen production from water under visible light. *Nat. Mater.* **8**, 76 (2009).

42. Perdew, J. P. Generalized gradient approximation made simple. *Phys. Rev. Lett.* **77**, 3865–3868 (1996).

43. Kresse, G. & Furthmüller, J. Efficient iterative schemes for ab initio total-energy calculations using a plane-wave basis set. *Phys. Rev. B.* **54**, 11169–11186 (1996).

Author contributions

D.W. S., B.H.L. and G.X.W. conceived and designed this work; X.C.G. performed the experiments and wrote the manuscript. B.H.L. and D.Z. contributed to the assembly of prototype soft-package Li-S batteries. W.J.W. and Y.C. contributed to the revision of the manuscript. All the authors discussed the results and participated in the preparation of the paper.

Additional information

Supplementary information accompanies this paper at https://doi.org/10.1038/s42004-019-0166-8.

Competing interests: The authors declare no competing interests.

Reprints and permission information is available online at http://npg.nature.com/reprintsandpermissions/

Publisher's note: Springer Nature remains neutral with regard to jurisdictional claims in published maps and institutional affiliations.